Flux growth and physical properties characterizations of Y1.866Eu0.134O3 and Lu1.56Gd0.41Eu0.03O3 single crystals

Philippe Veber, Matias Velazquez, Paul-Antoine Douissard, Thierry Martin, Olivier Plantevin, Rekia Belhoucif

Flux growth and physical properties characterizations of $Y_{1.866}Eu_{0.134}O_3$ and $Lu_{1.56}Gd_{0.41}Eu_{0.03}O_3$ single crystals

Philippe Veber,[1] Matias Velazquez,[1,*] Paul-Antoine Douissard,[2] Thierry Martin,[2] Olivier Plantevin,[3] and Rekia Belhoucif[4,5]

[1] *CNRS, Université de Bordeaux, ICMCB, 87 avenue du Dr. A. Schweitzer, 33608 Pessac cedex, France*
[2] *ESRF, The European Synchrotron, Instrumentation Services and Development Division, Detector Unit, 71 Avenue des Martyrs, 38043 Grenoble, France*
[3] *CSNSM UMR 8609, CNRS-Université d'Orsay, Bât. 108, 91405 Orsay Campus, France*
[4] *Faculté de Physique, Laboratoire d'Électronique Quantique, USTHB, BP 32 El alia, 16111 Bab Ezzouar, Alger, Algeria*
[5] *Faculté des Sciences, Département de Physique, UMBB, Boumerdes, Algeria*
[*] *matias.velazquez@icmcb-bordeaux.cnrs.fr*

Abstract: $Y_{1.866}Eu_{0.134}O_3$ and $Lu_{1.56}Gd_{0.41}Eu_{0.03}O_3$ single crystals of the cubic rare-earth sesquioxide phase were grown for the first time by a new flux method, in air and at temperatures between 1250 and 1100°C. Magnetic susceptibility measurements performed in the former crystals suggest that a preferential dissolution of Eu^{3+} cations occurs on the C_2-site. Transmission measurements established the promising optical quality of the samples, especially for $Lu_{1.56}Gd_{0.41}Eu_{0.03}O_3$ in the red spectral range where most of the scintillation light is emitted. The $Lu_{1.56}Gd_{0.41}Eu_{0.03}O_3$ single crystal, grown and tested for the first time, is an efficient X-ray scintillator and its characteristics seem promising for X-ray imaging with medium spatial resolution, in terms of light output and low afterglow. Emission and transmission spectra were measured and Eu^{3+} Judd-Ofelt analysis was performed in both crystals.

OCIS codes: (040.6070) Solid state detectors; (140.3380) Laser materials; (140.5680) Rare earth and transition metal solid-state lasers; (160.1890) Detector materials; (160.5690) Rare-earth-doped materials.

References and links

1. B. Lu, J.-G. Li, and Y. Sakka, "Controlled processing of $(Gd,Ln)_2O_3$:Eu (Ln=Y, Lu) red phosphor particles and compositional effects on photoluminescence," Sci. Technol. Adv. Mater. **14**(6), 064202 (2013).
2. D. J. Seo, Y. C. Kang, and S. B. Park, "The synthesis of $(Y_{1-x}Gd_x)_2O_3$:Eu phosphor particles by flame spray pyrolysis with LiCl flux," Appl. Phys., A Mater. Sci. Process. **77**(5), 659–663 (2003).
3. A. V. Strel'tsov, G. V. Torgashov, N. I. Sinitsyn, I. G. Torgashov, Yu. V. Gulyaev, V. P. Dmitrienko, and A. O. Dmitrienko, "Phase Composition and Luminescent Characteristics of Y_2O_3:Eu and Y_2O_2S:Eu Crystals Obtained using Borate Flux," IEEE International Conference on Vacuum Electronics 7th and IEEE International Conference on Vacuum Electron Sources 6th, Monterey, California, USA, 397–398, (2006).
4. Y. C. Kang, H. S. Roh, S. B. Park, and H. D. Park, "Use of LiCl flux in the preparation of Y_2O_3:Eu phosphor particles by spray pyrolysis," J. Eur. Ceram. Soc. **22**(9-10), 1661–1665 (2002).
5. S. Bär, G. Huber, J. Gonzalo, A. Perea, A. Climent, and F. Paszti, "Europium-doped sesquioxide thin films grown on sapphire by PLD," Mater. Sci. Eng. B **105**(1-3), 30–33 (2003).
6. A. Garcia-Murillo, C. Le Luyer, C. Dujardin, T. Martin, C. Garapon, C. Pédrini, and J. Mugnier, "Elaboration and scintillation properties of Eu^{3+}-doped Gd_2O_3 and Lu_2O_3 sol–gel films," Nucl. Instrum. Methods Phys. Res. A **486**(1-2), 181–185 (2002).
7. J. Zeler, L. B. Jerzykiewicz, and E. Zych, "Flux-Aided Synthesis of Lu_2O_3 and Lu_2O_3:Eu—Single Crystal Structure, Morphology Control and Radioluminescence Efficiency," Materials (Basel) **7**(10), 7059–7072 (2014).
8. N. A. Dulina, Y. V. Yermolayeva, A. V. Tolmachev, Z. P. Sergienko, O. M. Vovk, E. A. Vovk, N. A. Matveevskaya, and P. V. Mateychenko, "Synthesis and characterization of the crystalline powders on the basis of Lu_2O_3:Eu^{3+} spherical submicron-sized particles," J. Eur. Ceram. Soc. **30**(7), 1717–1724 (2010).

#247572 Received 7 Aug 2015; revised 22 Sep 2015; accepted 6 Oct 2015; published 18 Dec 2015

9. V. Peters, A. Bolz, K. Petermann, and G. Huber, "Growth of high-melting sesquioxides by the heat exchanger method," J. Cryst. Growth **237–239**, 879–883 (2002).
10. C. D. McMillen and J. W. Kolis, "Hydrothermal single crystal growth of Sc_2O_3 and lanthanide-doped Sc_2O_3," J. Cryst. Growth **310**(7-9), 1939–1942 (2008).
11. J. Sanghera, W. Kim, G. Villalobos, B. Shaw, C. Baker, J. Frantz, B. Sadowski, and I. Aggarwal, "Ceramic Laser Materials," Materials (Basel) **5**(12), 258–277 (2012).
12. A. Yoshikawa and V. Chani, "Growth of optical crystals by the micro-pulling-down method," MRS Bull. **34**(4), 266–270 (2009).
13. P. Veber, M. Velázquez, V. Jubera, S. Pechev, and O. Viraphong, "Flux growth of Yb^{3+}-doped RE_2O_3 (RE=Y,Lu) single crystals at half their melting point temperature," CrystEngComm **13**(16), 5220–5225 (2011).
14. G. Buşe, M. Velázquez, P. Veber, V. Jubera, Y. Petit, S. Péchev, O. Viraphong, R. Decourt, A. Jaffres, P. Aschehoug and G. Aka, "Spectroscopic properties of newly flux grown RE_2O_3:Yb^{3+} (RE=Y,Lu) laser crystals for high-power diode-pumped systems," Proc. SPIE, 8433 Solid State Lasers XXI: Technology and Devices **8433**, 84331B1–7 (2012).
15. M. Velázquez, P. Veber, G. Buşe, Y. Petit, P. Goldner, V. Jubera, D. Rytz, A. Jaffres, M. Peltz, V. Wesemann, P. Aschehough, and G. Aka, "Spectroscopic properties of newly flux grown and highly Yb^{3+}-doped RE_2O_3:Yb^{3+} (RE=Y,Gd,Lu) laser crystals," Opt. Mater. **39**, 258–264 (2015).
16. F. Druon, M. Velázquez, P. Veber, S. Janicot, O. Viraphong, G. Buşe, M. A. Ahmed, T. Graf, D. Rytz, and P. Georges, "Laser demonstration with highly doped Yb^{3+}:Gd_2O_3 and Yb^{3+}:Y_2O_3 crystals grown by an original flux method," Opt. Lett. **38**(20), 4146–4149 (2013).
17. P. Veber, M. Velázquez, G. Gadret, D. Rytz, M. Peltz, and R. Decourt, "Flux growth at 1230°C of cubic Tb_2O_3 single crystals and characterization of their optical and magnetic properties," CrystEngComm **17**(3), 492–497 (2015).
18. E. Castel, P. Veber, M. Albino, M. Velázquez, S. Péchev, D. Denux, J.-P. Chaminade, M. Maglione, and M. Josse, "Crystal growth and characterization of Tetragonal Tungsten Bronze ferroniobates $Ba_2LnFeNb_4O_{15}$," J. Cryst. Growth **340**(1), 156–165 (2012).
19. R. Belhoucif, M. Velázquez, Y. Petit, O. Pérez, B. Glorieux, O. Viraphong, P. de Marcillac, N. Coron, L. Torres, E. Véron, A. Kellou, P. Veber, R. Decourt, and H. El Hafid, "Growth and spectroscopic properties of ^{6}Li- and ^{10}B-enriched crystals for heat-scintillation cryogenic bolometers used in the rare events searches," CrystEngComm **15**(19), 3785–3792 (2013).
20. R. Belhoucif, M. Velazquez, Y. Petit, O. Plantevin, M. A. Couto dos Santos, F. Adamietz, V. Rodriguez, M. Couzi, O. Pérez, O. Viraphong, P. Veber, D. Denux, R. Decourt, and D. Ouadjaout, "Anisotropy of the spectroscopic, optical and thermo-mechanical properties of $Li_6Eu_{1-x}Gd_x(BO_3)_3$ crystals optimized for heat-scintillation cryogenic bolometers," Opt. Mater. Express **4**(10), 2042–2065 (2014).
21. M. Velázquez, A. Ferrier, J.-P. Chaminade, B. Menaert, and R. Moncorgé, "Growth and thermodynamic characterization of pure and Er-doped KPb_2Cl_5," J. Cryst. Growth **286**(2), 324–333 (2006).
22. A. Ferrier, M. Velázquez, X. Portier, J.-L. Doualan, and R. Moncorgé, "Tl_3PbBr_5: a possible crystal candidate for middle infrared nonlinear optics," J. Cryst. Growth **289**(1), 357–365 (2006).
23. N. C. Chang, "Fluorescence and stimulated emission from trivalent europium in yttrium oxide," J. Appl. Phys. **34**(12), 3500–3504 (1963).
24. M. Nikl, "Scintillation detectors for X-rays," Meas. Sci. Technol. **17**(4), 37–54 (2006).
25. T. Martin and A. Koch, "Recent developments in X-ray imaging with micrometer spatial resolution," J. Synchrotron Radiat. **13**(Pt 2), 180–194 (2006).
26. Z. Seeley, N. Cherepy, and S. Payne, "Two-step sintering of $Gd_{0.3}Lu_{1.6}Eu_{0.1}O_3$ transparent ceramic scintillator," Opt. Mater. Express **3**(7), 908–912 (2013).
27. R. P. Leavitt, J. B. Gruber, N. C. Chang, and C. A. Morrison, "Optical spectra, energy levels, and crystal-field analysis of tripositive rare-earth ions in Y_2O_3. II. Non-Kramers ions in C_2 sites," J. Chem. Phys. **76**(10), 4775–4788 (1982).
28. P. Caro and P. Porcher, "The paramagnetic susceptibility of C-type europium sesquioxide," J. Magn. Magn. Mater. **58**(1-2), 61–66 (1986).
29. C. Linarès, "Optical spectra and crystal field of the Europium(III) ion in some rare-earth metal oxide," J. Phys. **29**(10), 917–925 (1968).
30. R. Mokso, D. A. Schwyn, S. M. Walker, M. Doube, M. Wicklein, T. Müller, M. Stampanoni, G. K. Taylor, and H. G. Krapp, "Four-dimensional in vivo X-ray microscopy with projection-guided gating," Sci. Rep. **5**, 8727 (2015).
31. A. Rack, F. García-Moreno, T. Baumbach, and J. Banhart, "Synchrotron-based radioscopy employing spatio-temporal micro-resolution for studying fast phenomena in liquid metal foams," J. Synchrotron Radiat. **16**(Pt 3), 432–434 (2009).
32. J. Sun, P. Liu, S. Irvine, B. Pinzer, M. Stampanoni, and L. X. Xu, "Preliminary comparison of grating-based and in-line phase contrast X-ray imaging with Synchrotron radiation for mouse kidney at TOMCAT," J. Instrum. **8**(06), C06003 (2013).
33. J. M. Ogieglo, "Luminescence and energy transfer in garnet scintillators," PhD Thesis, University of Utrecht, The Netherlands, (2010).
34. Adachi Gy and N. Imanaka, "The binary rare-earth oxides," Chem. Rev. **98**(4), 1479–1514 (1998).

#247572 Received 7 Aug 2015; revised 22 Sep 2015; accepted 6 Oct 2015; published 18 Dec 2015

35. Z. M. Seeley, Z. R. Dai, J. D. Kuntz, N. J. Cherepy, and S. A. Payne, "Phase stabilization in transparent Lu_2O_3:Eu ceramics by lattice expansion," Opt. Mater. **35**(1), 74–78 (2012).
36. O. Knacke, O. Kubaschewski, and K. Hesselmann, eds., *Thermochemical Properties of Inorganic Substances,* 2nd Edition (Springer-Verlag, Vols. I and II, 1991).
37. I. Barin and G. Platzki, *Thermochemical Data of Pure Substances*, 3rd edition (VCH, Vol. I and II, 1995).

1. Introduction

Broadly speaking, the interest in synthesizing in different shapes rare-earth sesquioxides of the cubic phase is related to the diverse range of applications which can be envisioned from these materials: phosphor powders [1–4], scintillating thin films or powder materials [5–8], photonic nanomaterials, high-power and/or sub-100 fs lasers, eyesafe telecommunications lasers, yellow-orange-red solid state lasers, upconverter materials for the 3rd generation of photovoltaïc cell, and the list is not exhaustive [9–11]. The growth of rare-earth sesquioxides bulk single crystals is recognized as one of the most challenging endeavours of today's crystal growth, in the sense defined by these two science drivers: to produce well-established crystalline materials with improved quality and larger size at a lower cost ; to grow in bulk new categories of materials with extreme thermodynamic characteristics. Owing to both the extreme thermodynamic characteristics in which their growth takes place and a complex crystallographic polymorphism upon cooling, cubic rare-earth sesquioxides single crystals with improved quality and large size are difficult –if not still impossible– to obtain, especially at a lower cost [12]. In recent years, we have developed a cheap and user friendly flux growth process that works at half the melting temperature of rare-earth sesquioxides (between 1225 and 1130°C), and established that the new solvent it uses favours the crystallization of the cubic Gd_2O_3, Y_2O_3 and Lu_2O_3 phases with unprecedented Yb^{3+}-substitution levels without resorting to any post-growth thermal treatment [13]. The spectroscopic properties and laser operation based on these crystals have been investigated and found to be encouraging from the viewpoints of high-power and/or sub-100 fs pulse laser applications [14–16]. In addition to the first cubic Gd_2O_3:Yb^{3+} single crystals ever grown to date, pure Tb_2O_3 single crystals have been grown with promising Faraday rotation properties. Indeed, these heretofore unknown crystals displayed a Verdet constant ≈3.35 times higher than that of well-known commercial TGG crystals at 1064 nm, and an absorption coefficient (corrected for Fresnel reflexion losses) at the same wavelength ≈0.28 cm^{-1}, still too high to comply with industrial specifications for Faraday rotators but nevertheless quite encouraging [17]. They also proved to be fully Tb^{3+} reduced crystals by thermodynamic response functions (specific heat and magnetic susceptibility) measurements and analysis.

In this work we follow our exploration of the discovery potential of our growth process, by addressing the growth of Eu^{3+}-doped rare-earth sesquioxides. This oxidation state turns out to be even more reducible to Eu^{2+} than Yb^{3+} to Yb^{2+} in most oxides, chlorides and bromides [18–22]. We focused our efforts on the Y_2O_3:Eu^{3+} and $(Lu,Gd)_2O_3$:Eu^{3+} solid solutions for several reasons. The former one is the only one known to date and "historical" crystal that proved laser operation based on Eu^{3+} cations [23]. Moreover, its hexagonal $P6_3/mmc$ to cubic Ia-3 phase transition upon cooling makes it difficult to obtain optical quality and laser grade materials by classical high-temperature (≈2400-2500°C) solidification methods (heat-exchanger method, laser-heated pedestal growth or micro-pulling down), that is, directly from the molten state of the same composition. Indeed, such high-temperature methods use Re crucibles the stability of which requires to flow a mixture of gases containing explosive and highly reductive H_2. Our flux growth process was found to be operative in air, with Pt crucibles and a solvent completely devoid of OH^--groups, heavy metals (Pb, Bi, etc.) or any corrosive species. The interest in $(Lu,Gd)_2O_3$:Eu^{3+} lies in its potential X-ray imaging applications which are being developed at the ESRF, because of its high volumic mass (≈9 g/cm^3) and high average effective Z [24–26]. Eu^{3+} was chosen as an optically active cation because its well-known luminescent and scintillating properties [1–8,27] occur mainly in the orange-red spectral range, where cheap and almost 100% efficient detectors exist.

#247572 Received 7 Aug 2015; revised 22 Sep 2015; accepted 6 Oct 2015; published 18 Dec 2015

2. Experimental procedures

All the raw materials (Lu_2O_3, Gd_2O_3 and Eu_2O_3) were commercial powders of 5N purity, dried in air at 500°C during 12h, and 1000°C during 12h. The crystal growth of $(Lu_{0.5}Gd_{0.5})_2O_3:Eu^{3+}$ using a $Li_6(Lu_{0.475}Gd_{0.475}Eu_{0.05})(BO_3)_3$ solvent was performed in several stages. At first, a solute of formula $(Lu_{0.475}Gd_{0.475}Eu_{0.05})_2O_3$ was prepared by reacting together a stoichiometric and mechanically mixed amount of Lu_2O_3, Gd_2O_3 and Eu_2O_3 powders. Then, the $Li_6(Lu_{0.475}Gd_{0.475}Eu_{0.05})(BO_3)_3$ solvent was synthesized by mechanically mixing and grinding stoichiometric amounts of Li_2CO_3, H_3BO_3, Lu_2O_3, Gd_2O_3 and Eu_2O_3 powders, which were subsequently heated in air in a Pt crucible at 450°C during 12h, and at 750°C during 12h. The resulting mixture was then ground again in an agate mortar. Finally, a growth load composed of 124.9781 g (80 mol. %) of solvent $Li_6(Lu_{0.475}Gd_{0.475}Eu_{0.05})(BO_3)_3$ and 30.7919 g (20 mol. %) of solute $(Lu_{0.475}Gd_{0.475}Eu_{0.05})_2O_3$ was mechanically mixed and ground together. Melting of this mixture in air in a Pt crucible was performed at 1225°C. By means of a Pt and alumina double reflector (thickness higher than 1 mm for Pt and 2 mm for alumina), typical thermal gradients in the furnace can be reduced to $1°C.cm^{-1}$, so that the temperature distribution inside the molten charge remains as uniform as possible. Growth was initiated on a Pt spatula immersed into the melt. The molten bath stirring was undertaken by rotating the alumina rod at 30 rpm during 24h at 1225°C in order to dissolve completely the solute and homogenize the melt composition. Then, the Pt spatula was lifted in such a way as to maintain it a few millimeters below the melt surface, right at the center of the crucible section. In order to avoid sedimentation of the possibly remaining undissolved solute particles, a 20 rpm rotation was kept during the growth stage itself. The slow cooling of the flux was performed with a "shark teeth" profile at $-0.2°C.h^{-1}$ between 1225°C and 1130°C. At this temperature, the spatula was removed from the molten bath, and then the whole setup was allowed to cool down to 850°C at $6.5°C.h^{-1}$, and then at $30°C.h^{-1}$ down to room temperature. The alumina rod resisted quite well and just required cleansing in a diluted HCl solution to be fully operational for the next experiment.

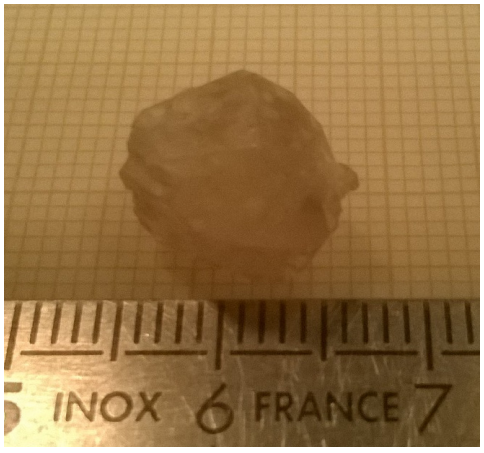

Fig. 1. As-grown $(Lu,Gd,Eu)_2O_3$ bulk single crystal (~0.5 cm^3) obtained by the flux method.

22 facets could be identified on the crystal shown in Fig. 1, among which two hexagonal ones, a majority of distorted diamond ones, and a small square one. 21 of the 22 facets could be oriented by the Laue method on a Delta Technologies International GM WS Series X-Ray goniometer head and found to be (211) planes. Interestingly, the small square facet was found to be (100). As the four largest d_{hkl}-spacings in this crystal are $d_{100}>d_{200}>d_{211}>d_{220}$, we conclude that the crystal grew close to equilibrium but that it was removed from the molten bath too early to observe a full equilibrium habit made of (100) facets. These observations are

#247572 Received 7 Aug 2015; revised 22 Sep 2015; accepted 6 Oct 2015; published 18 Dec 2015

similar to those already made in Yb^{3+}-doped Gd_2O_3, Y_2O_3 and Lu_2O_3 crystals and in pure Tb_2O_3 crystals [13,17].

Gd- and Eu-concentration were measured by scanning (211) facets, at a depth down to 2 µm, by means of EPMA (Cameca SX 100, 20 keV electron beam), and found to be independent on the spatial coordinates. In $Lu_{2-x-y}Gd_xEu_yO_3$ crystals, we found x = 0.41 (≈5.69 10^{21} Gd.cm^{-3}) and y = 0.03 (≈4.16 10^{20} Eu.cm^{-3}), whereas for the $Y_{2-x}Eu_xO_3$ crystal, we got x = 0.134 (≈1.79 10^{21} Eu.cm^{-3}). These amounts of substituents dissolved in their respective crystalline structures permit to estimate some effective and average distribution coefficient for each of them: $k_{av}(Gd^{3+})$≈0.43 and $k_{av}(Eu^{3+})$≈0.3 in Lu_2O_3, and $k_{av}(Eu^{3+})$≈0.67 in Y_2O_3. This trend in effective and average distribution coefficients can be correlated to the differences in ionic radii. Indeed, the difference in ionic radii between Eu^{3+} and Y^{3+} is smaller than that between Gd^{3+} and Lu^{3+}, which in turn is smaller than that between Eu^{3+} and Lu^{3+}.

Optical transmittance of the $Lu_{1.56}Gd_{0.41}Eu_{0.03}O_3$ (t = 360 µm) and $Y_{1.866}Eu_{0.134}O_3$ (t = 350 µm) unoriented single crystals from 200 to 3000 nm was recorded with a Cary 5000-UV-vis-NIR spectrometer and a resolution of 1 nm. The baseline difference between the two samples is likely to be due to the fact that owing to smaller dimensions of the $Y_{1.866}Eu_{0.134}O_3$ crystal (2x2 mm^2 section), the aperture angle was smaller. The emission spectrum at room temperature was measured with a Triax 320 spectrophotometer from Horiba-Jobin Yvon equipped with a PM Hamamatsu R928 detector and a resolution of 0.2 nm. The light excitation was delivered by an intense Xe lamp connected to a monochromator for spectral selection.

Magnetic susceptibility was measured in field-cooled mode using a Quantum Design SQUID MPMS XL magnetometer operated in the 4.2–354 K temperature range under an applied magnetic field of 1 mT for the flux-grown $Lu_{1.56}Gd_{0.41}Eu_{0.03}O_3$ crystal of mass 45.1 mg, and 8 mT for the flux-grown $Y_{1.866}Eu_{0.134}O_3$ crystal of mass 17.8 mg, both mounted in a capsule placed in a straw. The negligibly small diamagnetic contribution of the capsule was not subtracted from our data.

The X-ray conversion efficiency was measured with a monochromatic 8 keV energy X-ray beam produced by a lab X-ray generator (copper anode with 25 µm copper filter). Bulk YAG:Ce was used as a reference for the conversion efficiency measurement (conversion efficiency of bulk YAG:Ce = 100%). The scintillators were coupled to an X-ray microscope equipped with an Olympus 2x magnification microscope objective and a PCO Sensicam SVGA camera. The conversion efficiency was calculated from the flat field image (dark image corrected) obtained under 30 s exposure. The mean ADU signal extracted from a Region Of Interest (ROI) of the image was measured and corrected by the crystal absorption efficiency (crystal thickness) and the CCD camera spectral matching factor (convolution of scintillator emission spectrum and CCD sensor quantum efficiency).

The scintillation spectrum was measured under X-ray excitation energy of 8 keV with a copper anode. The spectrophotometer consisted of a CP140 Jobin Yvon monochromator coupled to a PCO2000 camera. The spectrum was corrected by the monochromator grating efficiency and the CCD camera Quantum Efficiency (QE).

The time response of the scintillators down to relative amplitudes of 10^{-5}–10^{-4} was studied since a dynamic range of up to 14 bits for successive images is required in some X-ray imaging applications. The afterglow decay depends on the exposure time and more slightly on the X-ray photon flux. Typical exposure times on synchrotron sources for X-ray tomography are 0.1–10 s (monochromatic X-ray beam up to 10^{13} photons/(s.mm^2)). The afterglow was measured at 8 keV with an X-ray tube equipped with a copper anode and copper filter. This corresponds to an X-ray photon flux of 10^6 photons/(s.mm^2), which is considerably lower than the synchrotron beam intensity. The signal decay was measured with a PMT 2020Q coupled to a SR445 Stanford Research amplifier and a SR400 gated photon counter from Stanford Research Instrument working in counting mode and sampled at intervals of 4 ms.

#247572 Received 7 Aug 2015; revised 22 Sep 2015; accepted 6 Oct 2015; published 18 Dec 2015

3. Emission spectra and Judd-Ofelt analysis

The average refractive index was assumed to be 1.9 for both crystals, and was used for all the spectral range investigated to calibrate the spectra by the Fuchtbauer-Ladenburg method. The stimulated emission cross section for a given transition from state J to state J_0 can be evaluated by the following expression:

$$\sigma_{EM} = \frac{1}{8\pi cn^2}\beta_R \frac{1}{\tau_R}\lambda^5 \frac{I_{EM}(\lambda)}{\int \lambda I_{EM}(\lambda) d\lambda} \quad (1)$$

in which c, n, β_R, τ_R, λ and I_e symbolize the speed of light, the average refractive index, the branching ratio, the radiative lifetime, the wavelength and the emission intensity, respectively. The room temperature emission spectrum of the two crystals after excitation into the $^5L_6$ (393 nm) levels are shown in Fig. 2. The intensities of the emission occurring exclusively from the $^5D_0$ level is relatively high, and were assigned to $^5D_4$-^7F_J (J = 0-5) transitions, both spin and parity forbidden. From shorter to longer emission wavelengths, the most intense transition is the hypersensitive $^5D_0$-$^7F_2$ transition centered at 610.4 nm, with a $\sigma_{EM} \approx 1.71 \times 10^{-20}$ cm^2 and $\approx 1.12 \times 10^{-20}$ cm^2, in $Y_{1.866}Eu_{0.134}O_3$ and $Lu_{1.56}Gd_{0.41}Eu_{0.03}O_3$ crystals, respectively. As compared to the similar ones observed in $Li_6Eu_{1-x}Gd_x(BO_3)_3$ (x = 0, 0.25 and 0.35) crystals, this transition is slightly blue-shifted and more intense [19,20].

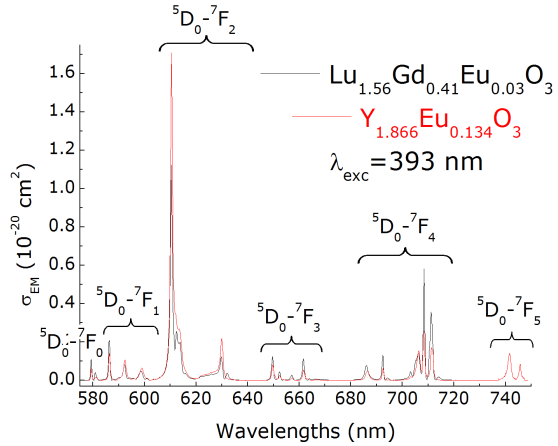

Fig. 2. FL-calibrated stimulated emission cross-section of the $Y_{1.866}Eu_{0.134}O_3$ and $Lu_{1.56}Gd_{0.41}Eu_{0.03}O_3$ crystals at room temperature under excitation at 393 nm.

The number of crystal-field sublevels shown in the emission spectra indicates a complete degeneracy lifting consistent with the C_2 site symmetry adopted by ~¾ of the Eu^{3+} ions. We performed the Judd-Ofelt analysis to estimate the intensity parameters Ω_λ (λ = 2,4) exactly as in [19] and [20], by using the ratio of the integrated intensity of the $^5D_0 \rightarrow {}^7F_{2,4}$ electric dipole transitions, $\int I_J(\nu)d\nu$, to the integrated intensity of the $^5D_0 \rightarrow {}^7F_1$ purely magnetic dipole transition, $\int I_1(\nu)d\nu$. The Judd-Ofelt parameters, oscillator strengths, spontaneous emission probabilities, branching ratios, ratio "R" of integrated emission intensity of the hypersensitive transition $^5D_0 \rightarrow {}^7F_2$ to that of the $^5D_0 \rightarrow {}^7F_1$ magnetic transition, and radiative lifetimes are gathered in Table 1.

#247572 Received 7 Aug 2015; revised 22 Sep 2015; accepted 6 Oct 2015; published 18 Dec 2015

Table 1. Results of the Judd-Ofelt analysis carried out in the $Y_{1.866}Eu_{0.134}O_3$ (A) and $Lu_{1.56}Gd_{0.41}Eu_{0.03}O_3$ (B) single crystals: energy barycenter ν, $\Omega_{2,4}$ JO parameters, electric and magnetic oscillator strength (*f*), radiative transition rates (A_R), branching ratios (β_R), radiative lifetimes (τ_R).

Crystal	Transition	ν (cm^{-1})	Ω_2 ($\times 10^{-20}$ cm^2)	Ω_4 ($\times 10^{-20}$ cm^2)	f ($\times 10^{-6}$)	A_R (s^{-1})	β_r (%)	R	τ_R (ms)
A	$^5D_0 \rightarrow {}^7F_0$	17261.1	11.21	4.66	0.018	12.95	1.24	7.5	0.987
	$^5D_0 \rightarrow {}^7F_1$	16877.1			0.14	99.21	9.50		
	$^5D_0 \rightarrow {}^7F_2$	16296.2			1.16	745.88	71.43		
	$^5D_0 \rightarrow {}^7F_3$	15262.7			0.063	35.72	3.42		
	$^5D_0 \rightarrow {}^7F_4$	14193.7			0.3	147.32	14.11		
	$^5D_0 \rightarrow {}^7F_5$	13468.6			0.0098	3.00	0.28		
B	$^5D_0 \rightarrow {}^7F_0$	17262.2	7.34	5.58	0.034	24.25	2.88	4.9	1.19
	$^5D_0 \rightarrow {}^7F_1$	16913.9			0.14	99.86	11.86		
	$^5D_0 \rightarrow {}^7F_2$	16294.1			0.76	487.98	57.97		
	$^5D_0 \rightarrow {}^7F_3$	15241.1			0.095	53.22	6.32		
	$^5D_0 \rightarrow {}^7F_4$	14198.5			0.36	176.45	20.96		

The emission band for the $^5D_0$-$^7F_6$ transition, centered around 810 nm, could not be measured accurately because of limitations of our detector in this spectral range. We found that $\Omega_2 > \Omega_4$ for both crystals, exactly as in $Li_6Eu_{1-x}Gd_x(BO_3)_3$ solid solution crystals [19,20]. The striking feature about Ω_2 lies in its high sensitivity to the covalence degree of the chemical bond: the more covalent the Eu-O chemical bond, the higher the Ω_2 value, the higher the contribution of the electric dipole mechanism, but also the lower the symmetry. Since it is very sensitive to the crystal field, the Ω_2 value changes greatly from compound to compound. The $^7F_1$ and $^7F_2$ multiplet crystal field splittings in the two crystals are consistent with previous energy level diagram determination and crystal field calculations [27–29]. The energy level positions of the lowest spin-orbit multiplets are given in Table 2

Table 2. Energy level positions determined at room temperature in the $Y_{1.866}Eu_{0.134}O_3$ (A) and $Lu_{1.56}Gd_{0.41}Eu_{0.03}O_3$ (B) single crystals.

Crystal	Transition	ν (cm^{-1})	Comment	Room temperature experimental energy (K)
A	$^5D_0 \rightarrow {}^7F_0$	17261.1 17207.6	C_2 C_{3i}	0 0
	$^5D_0 \rightarrow {}^7F_1$	17053.4 16881.5 16697.4	$^7F_1$ crystal-field sublevels	267.3 512.8 775.9
	$^5D_0 \rightarrow {}^7F_2$	16381.1 16338.1 16295.4 15971.7 15875.4	$^7F_2$ crystal-field sublevels	1227.8 1289.2 1350.3 1812.8 1950.4
B	$^5D_0 \rightarrow {}^7F_0$	17262.2 17212.2	C_2 C_{3i}	0 0
	$^5D_0 \rightarrow {}^7F_1$	17055.5 16887.3 16707.0	$^7F_1$ crystal-field sublevels	270.3 510.6 768.3
	$^5D_0 \rightarrow {}^7F_2$	16382.7 16327.5 16295.3 15881.6 15820.2	$^7F_2$ crystal-field sublevels	1231.5 1310.5 1356.5 1947.6 2035.3

4. Magnetic susceptibility behaviour

In cubic Eu_2O_3, Caro and Porcher firmly established the important contribution from the Eu^{3+} cations located in the C_{3i}-site to the total magnetic susceptibility [28]. The fact that in this

#247572 Received 7 Aug 2015; revised 22 Sep 2015; accepted 6 Oct 2015; published 18 Dec 2015

crystallographic site the lowest of the crystal field sublevels of the $^7F_1$ multiplet is noticeably low in energy (≈185 K) leads to a typical low temperature plateau of the Van Vleck paramagnetic behaviour which starts at lower temperature (≈32 K) and higher susceptibility value. Hence, the resulting average magnetic susceptibility displays a low temperature plateau which starts at lower temperature than if it was due only to the Eu^{3+} cations located in the C_2-site.

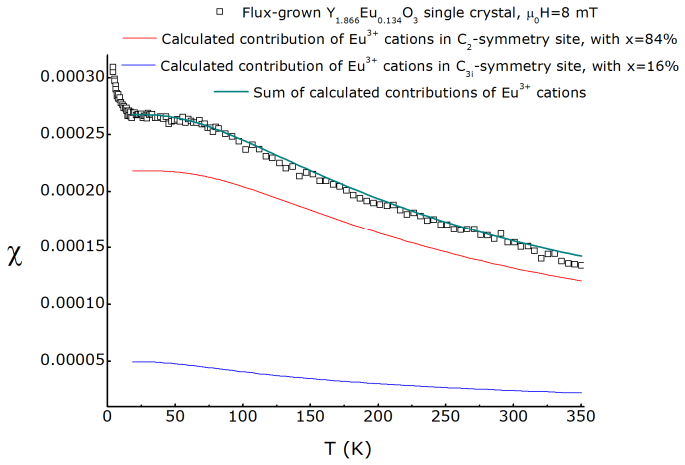

Fig. 3. MKSA magnetic susceptibility of an $Y_{1.866}Eu_{0.134}O_3$ flux-grown crystal. The energy level positions in the calculations were: C_2 symmetry, E_1 = 267.3 K, E_2 = 510 K, E_3 = 800 K and E_4 = 1750 K (adapted from Table 2) ; C_{3i} symmetry, E_1 = 183.3 K, E_2 = 714.4 K, E_3 = 714.4 K and E_4 = 1750 K (adapted from [28]).

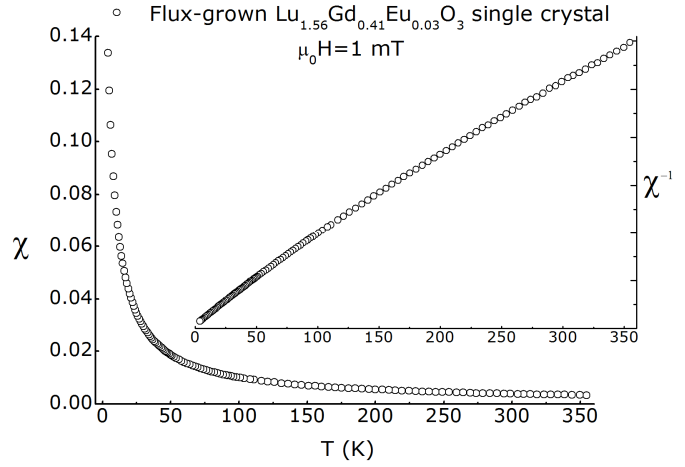

Fig. 4. MKSA magnetic susceptibility and inverse magnetic susceptibility of a $Lu_{1.56}Gd_{0.41}Eu_{0.03}O_3$ flux-grown crystal.

In Fig. 3, it is seen that $Y_{1.866}Eu_{0.134}O_3$ exhibits the typical Van Vleck paramagnetic behaviour (see [19] for a detailed phenomenological description) with the notable exception of the Curie-type tail at temperatures below ~16 K, which is likely to be due to some Gd^{3+} contamination and/or negligible Eu^{3+} reduction to Eu^{2+}. One interesting thing to observe is that the magnetic susceptibility plateau starts at a higher temperature upon cooling than the one of cubic Eu_2O_3 shown in [28]. Even if the overall crystal field strength is different in both compounds, the crystal field sublevels energy positions of the $^7F_1$ multiplet remains virtually the same in both cubic Eu_2O_3 and Y_2O_3:Eu^{3+} [27,28], and so our magnetic susceptibility data

#247572 Received 7 Aug 2015; revised 22 Sep 2015; accepted 6 Oct 2015; published 18 Dec 2015

suggests that in the flux-grown $Y_{1.866}Eu_{0.134}O_3$ crystals the Eu^{3+} cations distribution, which is expected to follow the ¾-C_2/¼-C_{3i} crystallographic landscape offered by the cubic structure, is shifted in favour of the C_2-symmetry site by a substantial amount, roughly ≈84%-C_2/16%-C_{3i}. When a ¾-¼ distribution is included in the magnetic susceptibility calculation, the low temperature plateau (fixed by the Eu^{3+} concentration, ≈1.79 10^{21} Eu.cm^{-3}) is clearly overestimated by an amount which compares to the error bar of the measurement. Neutron or XRD data refinement, or ^{151}Eu Mössbauer spectroscopy, would certainly help cross-checking this trend. Consequently, it seems that the liquid-solid partition coefficient is higher for the Eu^{3+} cations dissolved on the C_2-smmetry site in Y_2O_3. In Fig. 4, the $Lu_{1.56}Gd_{0.41}Eu_{0.03}O_3$ flux-grown crystal magnetic susceptibility behaviour could not be fitted to a Curie-Weiss law, a Van Vleck paramagnet law, nor a linear combination of both over the whole temperature range investigated. From 4.2 K to ~65 K, a reasonable Curie-Weiss fit could be obtained, leading to a Curie constant C≈0.983 K, a paramagnetic Curie temperature θ_p≈-3.2 K and an effective magnetic moment μ_{eff}≈8.13 μ_B/Gd^{3+}. The latter value corresponds to 102.4% of the theoretical Gd^{3+} free ion value and suggests that at low temperatures, where the Van Vleck paramagnetism of the Eu^{3+} cations is not expected to affect the temperature dependence of the overall magnetic susceptibility, the paramagnetism is dominated by the Gd^{3+} magnetic moments. At higher temperatures, the (tiny) deviation from the Curie-Weiss behaviour is likely to be due to the Van Vleck paramagnetism of Eu^{3+} cations. As a matter of fact, the three crystal field sublevels of the C_2-site Eu^{3+} cations $^7F_1$ multiplet were observed at 275, 538 and 824 K, and the first $^7F_2$ crystal field sublevel in the same site was observed at 1232 K [29]. The fact that no linear combination of Van Vleck and Curie-Weiss paramagnetisms could fit the data stresses the complexity of this paramagnetism. Indeed, given the high substitution levels, Gd^{3+} and Eu^{3+} magnetic moments are probably not independent from each other. In principle, there can be Gd(C_2)-Gd(C_2), Gd(C_2)-Gd(C_{3i}), Gd(C_{3i})-Gd(C_{3i}), Eu(C_2)-Gd(C_2), Eu(C_2)-Gd(C_{3i}), Eu(C_{3i})-Gd(C_2) and Eu(C_{3i})-Gd(C_{3i}) magnetic interactions, the Eu-Eu interactions being certainly negligible. In the $Li_6Eu_{1-x}Gd_x(BO_3)_3$ solid solution crystals, drastically different paramagnetic behaviours were also observed between the x = 0 and the x = 0.25 members [19] and such discrepancies (Van Vleck *versus* Curie-Weiss) are similar to those observed in the comparison between the $Lu_{1.56}Gd_{0.41}Eu_{0.03}O_3$ magnetic susceptibility and that of Y_2O_3:Eu^{3+} in Figs. 3 and 4.

5. Characterization of the $Lu_{1.56}Gd_{0.41}Eu_{0.03}O_3$ single crystal optical/scintillation properties

The $Lu_{1.56}Gd_{0.41}Eu_{0.03}O_3$ single crystal scintillation properties were characterized with a view to synchrotron X-ray imaging applications, with spatial resolutions in the ~2-25 µm range [30–32]. In this realm of applications, bulk $Y_3Al_5O_{12}$:Ce (YAG:Ce) and $Lu_3Al_5O_{12}$:Ce (LuAG:Ce) single crystals are currently reference materials [30–32]. These crystals exhibit a good tolerance to radiations, a good chemical (not hygroscopic) and mechanical stability, are easy to process with a good optical quality and can be polished down to thicknesses of 5 µm. However, YAG:Ce suffers from relatively low X-ray absorption efficiency. On the other side, LuAG:Ce displays higher stopping power and conversion efficiency, although it generally shows a high level of afterglow [33]. This is a problem when acquiring tomographic slices with high dynamic range.

In order to evaluate the scintillation properties of the $Lu_{1.56}Gd_{0.41}Eu_{0.03}O_3$ single crystal, the conversion efficiency, scintillation spectrum, UV-Visible transmission, afterglow and X-ray images were measured.

#247572 Received 7 Aug 2015; revised 22 Sep 2015; accepted 6 Oct 2015; published 18 Dec 2015

Table 3. Conversion efficiency of $Lu_{1.56}Gd_{0.41}Eu_{0.03}O_3$ crystal compared with YAG:Ce and LuAG:Ce reference crystals.

Sample	Crystal growth method	Thickness (μm)	X-ray Absorption efficiency	CCD camera Spectral matching factor	Conversion efficiency (%)	Conversion efficiency (ph/keV)
YAG:Ce	Czochralski	500	1	0.262	100	~18
LuAG:Ce	Czochralski	120	1	0.262	131	~24
$(Lu,Gd)_2O_3:Eu^{3+}$	Flux	500	1	0.254	200-250	~40-45

The $(Lu,Gd)_2O_3:Eu^{3+}$ conversion efficiency is very high. Some comparisons are drawn in Table 3, especially with LuAG:Ce which is a reference crystal used for X-ray imaging with medium spatial resolution in synchrotron facilities.

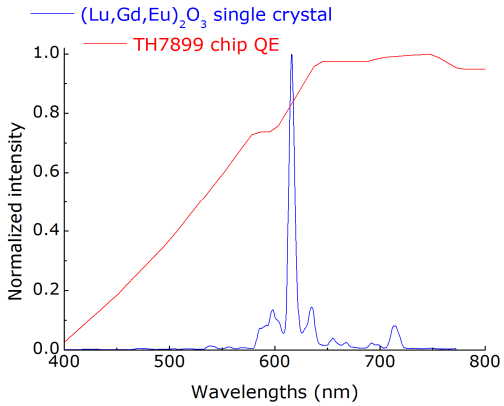

Fig. 5. $Lu_{1.56}Gd_{0.41}Eu_{0.03}O_3$ single crystal scintillation spectrum under X-ray excitation at 8 keV and matching with the atmel TH7899 Quantum Efficiency.

The scintillation spectrum of the $Lu_{1.56}Gd_{0.41}Eu_{0.03}O_3$ crystal shown in Fig. 5 displays several bands which, by comparison with Fig. 2, can be assigned to the Eu^{3+} cations intraconfigurational transitions $^5D_0 \rightarrow {}^7F_{0\text{-}5}$. The relative peak intensities seem to compare with those of Fig. 2, except for the $^5D_0 \rightarrow {}^7F_4$ emission, which is slightly decreased. The scintillation spectrum of $Lu_{1.56}Gd_{0.41}Eu_{0.03}O_3$ single crystals matches well the quantum efficiency wavelength dispersion of the Frelon 2k (equipped with the chip TH7899 atmel), and more broadly speaking is well adapted to front illuminated sensors.

#247572 Received 7 Aug 2015; revised 22 Sep 2015; accepted 6 Oct 2015; published 18 Dec 2015

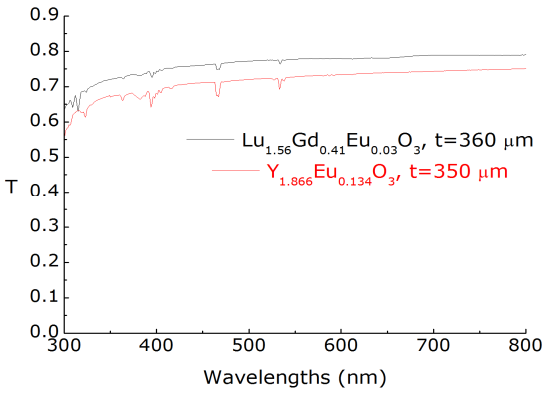

Fig. 6. Transmission spectra of $Lu_{1.56}Gd_{0.41}Eu_{0.03}O_3$ and $Y_{1.866}Eu_{0.134}O_3$ single crystals between 300 and 800 nm.

The transmission of the $Lu_{1.56}Gd_{0.41}Eu_{0.03}O_3$ crystal was found to be 0.65-0.79 and devoid of sharp absorption edge over the 300-800 nm spectral range (Fig. 6). By performing Fresnel reflection losses correction, with n = 1.9, we could roughly estimate that the absorption coefficient in the red spectral range is ~1.3 cm^{-1}. Moreover, using the energy levels position given in [29] to calculate the $^7F_2$ multiplet partition function (Z≈2.51, at room temperature), we can estimate by the reciprocity method that the absorption coefficient at 610.4 nm is ~1.8 cm^{-1}. Hence, the crystal does not reabsorb significantly the scintillation light (l_{ABS}~5500 μm) where it is the most intense and the detector proves to be the most efficient.

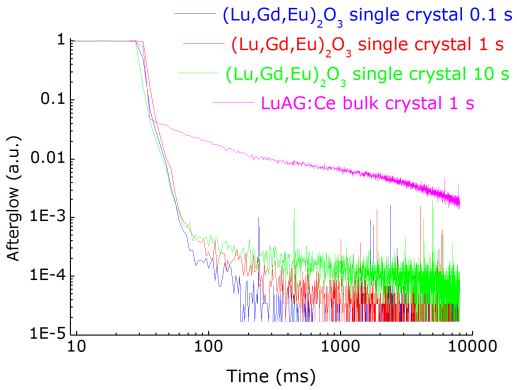

Fig. 7. Afterglow of $Lu_{1.56}Gd_{0.41}Eu_{0.03}O_3$ single crystal at 8 keV for different exposure times (0.1 s, 1 s and 10 s), and comparison with a bulk LuAG:Ce crystal exposed during 1 s to X-rays.

The afterglow at room temperature of the $Lu_{1.56}Gd_{0.41}Eu_{0.03}O_3$ crystal is low (Fig. 7). After ~100 ms, a dynamic range of 13 bits can be solved. The afterglow of the $Lu_{1.56}Gd_{0.41}Eu_{0.03}O_3$ crystal is lower than its ceramics analog [26] and also much lower than the LuAG:Ce single crystal. The afterglow in LuAG:Ce is attributed to vacancies, Lu-Al antisite defects or dislocations, which trap electron and holes, and then recombine non-radiatively [32]. This afterglow depends on the Ce concentration and that is why some discrepancies can arise from sample to sample in LuAG:Ce. An X-ray image with the $Lu_{1.56}Gd_{0.41}Eu_{0.03}O_3$ single crystal is shown in Fig. 8. It was difficult to reach a good focus with the $Lu_{1.56}Gd_{0.41}Eu_{0.03}O_3$ crystal. In comparison with standard YAG:Ce crystal, our $Lu_{1.56}Gd_{0.41}Eu_{0.03}O_3$ crystal clearly still have many defects with a size ranging from 1 to 20 μm.

The high melting temperature of rare-earth sesquioxides raises the question of the crucible and refractory materials to be used: Pt, Mo, W, Ir, alumina and magnesia have to be avoided.

#247572 Received 7 Aug 2015; revised 22 Sep 2015; accepted 6 Oct 2015; published 18 Dec 2015

So far, the best results have been achieved with expensive Re crucibles, pedestal, nozzles and top cap reflectors, which exhibit a propensity to oxidize in contact with the oxide-based refractory material and with the few ppm of oxygen flowing in the furnace, and also dissolve in molten Lu_2O_3 bath, forming ~20 μm-sized particles embedded in the resulting crystals. Re is too much expensive because its high mechanical hardness makes it difficult to shape in a specific form. The Re powder compaction process involved to obtain specifically shaped Re parts of the furnace, is also likely to introduce Fe and other undesired metallic optical contaminants. The chemical (and subsequently mechanical) stability of the Re parts requires a flux gas containing H_2 at ~2400°C, which entails health and safety requirements unlikely to favour large scale industrial production.

Moreover, for the rare-earth sesquioxydes preceding Yb_2O_3 in the periodic table, there exists structural phase transition, and even series of structural phase transitions, which make it impossible to obtain directly the cubic phase, or to obtain it with good (laser grade) crystal quality [34], as is the case for rare-earth doped Y_2O_3 crystals. If we calculate the average ionic radius on the rare-earth crystallographic sites in $Lu_{1.56}Gd_{0.41}Eu_{0.03}O_3$ and $Y_{1.866}Eu_{0.134}O_3$ crystals, we see that in Adachi and Imanaka's diagram, the former is in some sense « equivalent » to growing Ho_2O_3, and the latter « equivalent » to growing Dy_2O_3, so that there must be hexagonal $P6_3/mmc \rightarrow$ cubic Ia-3 and hexagonal $P6_3/mmc \rightarrow$ monoclinic $C2/m \rightarrow$ cubic Ia-3 phase transitions, especially in $Lu_{1.56}Gd_{0.41}Eu_{0.03}O_3$ [35]. The chemical, spectroscopic and magnetic characterizations presented in this work firmly establish that, for the first time, cubic $Lu_{1.56}Gd_{0.41}Eu_{0.03}O_3$ and $Y_{1.866}Eu_{0.134}O_3$ crystals could be grown at half their melting point temperature. At this temperature, the cubic phase stability domain is directly reached from the liquid state, and it is possible to take advantage of isotropic thermal, thermomechanical and thermo-optical behaviors of these crystals upon cooling. In addition, the growth process is favored by the fact that the crystals have higher thermal conductivity upon cooling, the liquid phase exhibits higher liquid surface tension and lower vapor pressure.

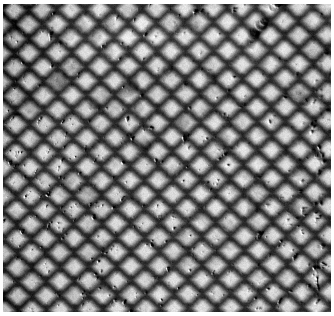

Fig. 8. X-ray resolution target image of the $Lu_{1.56}Gd_{0.41}Eu_{0.03}O_3$ crystal. The field view is 1.3x1.3 mm^2 and the grid lines thickness is ~25 μm.

The crystal growth takes place in air so that Eu^{3+} oxidation state can be stabilized without resorting to any post-growth thermal treatment annealing. As a matter of fact, the thermochemical data tables indicate [36,37] that the reduction temperature of Eu_2O_3 to EuO under an oxygen partial pressure of 10^{-7} atm is ~2400 K. Hence, melting Eu_2O_3 under a flow of gas containing hydrogen (P_{O2}~10^{-11} atm) will completely reduce it with formation of many gas bubbles in the melt. From an industrial viewpoint, one should also note that the solvent used contains neither heavy metal, hydroxyl groups nor corrosive species, and that the furnace scheme is the most simple one can conceive for flux growth, with easily found high purity Pt crucibles and spatula, cheap (Kanthal) resistive heating and alumina refractory elements. In spite of the huge body of literature dealing with Eu^{3+}-doped rare-earth sesquioxides and their spectroscopic properties, the availability of single crystals under "mild" conditions permitted us to obtain emission spectra calibrated in cross section units for the first time. Single crystals are the only objects which allow for the determination of intrinsic properties and of their

#247572 Received 7 Aug 2015; revised 22 Sep 2015; accepted 6 Oct 2015; published 18 Dec 2015

anisotropy, even in cubic phases, when the property under investigation depends on the direction or implies the orientation of some field with respect to the structural polyhedra relevant to it. In comparison with complex preparation processes [1,2,4,8,11], note that in our growth process, the microstructure of the starting powder is not a key parameter.

6. Conclusions

We have successfully grown a ~0.5 cm^3 $Lu_{1.56}Gd_{0.41}Eu_{0.03}O_3$ as well as smaller $Y_{1.866}Eu_{0.134}O_3$ sesquioxide single crystals of the cubic phase. The $Li_6(Lu,Gd,Eu)(BO_3)_3$ and $Li_6(Y,Eu)(BO_3)_3$ solvents that we used for the high-temperature solution growth makes it possible to obtain these crystals at half their melting temperature, in air, without resorting to any post-growth thermal annealing to stabilize the Eu^{3+} oxidation state. According to the Van Vleck paramagnetism observed in $Y_2O_3:Eu^{3+}$ crystals, the $Li_6(Y,Eu)(BO_3)_3$ solvent leads to a preferential dissolution of the Eu^{3+} cations on the C_2-site of the cubic Y_2O_3 crystal structure. Transmission measurements established the promising optical quality of the samples, especially for $Lu_{1.56}Gd_{0.41}Eu_{0.03}O_3$ in the red spectral range where most of the scintillation light is emitted. The $Lu_{1.56}Gd_{0.41}Eu_{0.03}O_3$ single crystal, grown and tested for the first time, is an efficient X-ray scintillator and its characteristics seem promising for X-ray imaging with medium spatial resolution, especially when it is coupled to such a front-illuminated CCD chip as atmel TH7899 2k with a maximum quantum efficiency between 620 nm and 800 nm. The $Lu_{1.56}Gd_{0.41}Eu_{0.03}O_3$ emission spectrum exhibits in the 575-750 nm spectral range, series to 4f-4f transitions arising from the Eu^{3+} cations, particularly well-suited to most CCD/CMOS cameras.

#247572 Received 7 Aug 2015; revised 22 Sep 2015; accepted 6 Oct 2015; published 18 Dec 2015